High-strength high-ductility Engineered/Strain-Hardening Cementitious Composites (ECC/SHCC) incorporating geopolymer fine aggregates

Ling-Yu Xu [a], Bo-Tao Huang [a,**], Victor C. Li [b], Jian-Guo Dai [a,*]

[a] Department of Civil and Environmental Engineering, The Hong Kong Polytechnic University, Hong Kong, China
[b] Department of Civil and Environmental Engineering, University of Michigan, Ann Arbor, USA

ARTICLE INFO

ABSTRACT

In this study, Engineered/Strain-Hardening Cementitious Composites (ECC/SHCC) incorporating geopolymer fine aggregates were successfully developed with high strength and high ductility. A multi-scale investigation was conducted to gain an in-depth understanding of the microstructure and ductility enhancement mechanism of geopolymer aggregate ECC (GPA-ECC). The use of geopolymer fine aggregates enabled the high-strength ECC to achieve higher tensile ductility and finer crack width compared to existing ones with similar compressive strength in the literature. It was found that the GPA reacted with the cementitious matrix, and the width of the GPA/matrix interfacial transition zone (ITZ) was larger than that of the silica sand/matrix ITZ. Moreover, the GPA achieved a strong bond with the cementitious matrix and could behave as "additional flaws" in high-strength matrix, resulting in saturated multiple cracking and excellent tensile ductility of ECC. This study provides a new avenue for developing high-performance fiber-reinforced cementitious composites based on artificial geopolymer aggregates.

1. Introduction

Engineered/Strain-Hardening Cementitious Composites (ECC/SHCC) are fiber-reinforced cement-based materials with tensile strain-hardening behavior and high ductility [1,2]. Based on the micromechanical design criteria [3,4], ECC are developed to overcome the quasi-brittle nature of conventional concrete materials and enhance the resilience and sustainability of civil infrastructures [5–7]. Generally, the compressive strengths of normal ECC range from 20 MPa to 80 MPa [8–10], and the tensile strain capacities vary within 1%–6% (100–600 times that of plain concrete) [11–13]. In recent years, increasing efforts have been focused on improving the compressive strength (e.g., over 120 MPa [14]), tensile ductility (e.g., over 8% [15]), and sustainability (e.g., using alternative binders [16]) of ECC materials to broaden their practical applications in civil infrastructures. According to the micromechanics of strain-hardening cement-based materials [1], fine silica sand is commonly used in both normal- and high-strength ECC. However, the cost of silica sand is significantly higher than that of natural river sand, and the exploitation of natural silica rocks also imposed a negative impact on the environment. To address such challenge, efforts

have been made to produce ECC materials with alternative fine aggregates (e.g., sea-sand [17], crumb rubber [18], iron ore tailings [19], waste glass [20] and recycled fine aggregates [21]).

Artificial aggregate is an emerging technology aiming to alleviate the shortage problem of natural aggregates [22,23]. Such aggregates are usually made from industrial wastes/by-products, and thus can help reduce the environmental burden caused by natural resources excavation and solid waste landfill [24], leading to an attractive one-stone two-bird solution. Generally, the artificial aggregates can be classified into three groups: sintered aggregates [25], traditional cold-bonded aggregates (i.e., using Portland cement as binder) [26], and geopolymer aggregates [27]. Among these technologies, sintered aggregates can achieve the best mechanical performance and the lightest weight, but the practical application of sintered aggregates is limited to a large extent due to the high energy consumption and cost of the sintering process (usually over 1000 °C). By contrast, traditional cold-bonded aggregates and geopolymer aggregates (GPA) can be produced at the ambient temperature, making them more economical for industrialization [26,28]. Considering the sustainability issue, GPA may provide a better option than traditional cold-bonded ones, as the

---

production of cementitious binders (e.g., Portland cement or hydrated lime) usually leads to higher carbon emission compared to most types of geopolymers [29], which is a critical problem resulting in the climate crisis today [30]. However, similar to the traditional cold-bonded aggregates, GPA are much weaker than natural aggregates in terms of the strength and modulus, which is a major limitation for their practical applications in concrete structures [31].

In this study, GPA were innovatively utilized as fine aggregates to fully replace fine silica sand in high-strength ECC materials with the following motivations. (1) Alkali-activation is an effective way to turn industrial/urban/agricultural by-products/wastes (e.g., coal fly ash [32], GGBS [33], rice husk ash [34], red mud [35], coal bottom ash [36], mine tailings [27], palm oil fuel ash [37], and peat-wood fly ash [38]) into environmentally-friendly geopolymer aggregates. (2) A strong interface was observed between alkali-activated fly ash/slag paste and Portland cement paste [39,40], indicating that GPA may exhibit excellent bond with cement-based matrix. (3) The comparatively low strength and modulus of GPA can be taken advantage of to reduce the cracking strength and to modify the fracture toughness of high-strength ECC matrix, which is beneficial for the saturated multiple cracking behavior of ECC under direct tension [41]. It is noted that the weakness of using artificial aggregates in ordinary concrete is usually associated with the reduced strength and modulus, but such weakness may be utilized to tailor the matrix of ECC to enhance their tensile ductility. Therefore, this paper explored the use of geopolymer fine aggregates to replace fine silica sand to tailor the ECC matrix properties.

A multi-scale investigation was conducted to understand the microstructures and tensile properties of high-strength ECC with different contents of GPA. First, the mechanical properties including the compressive strength, tensile behavior, and crack patterns of GPA-ECC were investigated. Second, in order to understand the mechanisms behind the properties, the reaction kinetics and the interfacial properties of the matrix incorporating GPA were analyzed based on the calorimetry test, Back Scattered Electron (BSE) with Energy Dispersive Spectroscopy (EDS), and microhardness test, as compared to its counterpart with silica sand. Finally, the internal cracking behavior and the size distributions of matrix flaws and geopolymer aggregates were analyzed by X-ray computed tomography (XCT), leading to an in-depth understanding of the cracking behavior of GPA-ECC.

2. Experimental program

2.1. Raw materials of artificial aggregate and ECC

Coal fly ash (FA) and Type I 52.5 N Portland cement used in the study, both provided by Green Island Cement Co. Ltd., Hong Kong, were used as the precursor for GPA production and the binder for ECC production, respectively. Ground granulated blast-furnace slag (GGBS) transported from Mainland China was also used as the supplementary precursor in artificial aggregate production to facilitate ambient curing of the GPA. Silica fume (SF) was used as the highly reactive supplementary cementitious material (SCM) in the preparation of high-strength ECC.

Table 1 presents the chemical compositions and loss on ignition (LOI) of the raw materials from x-ray fluorescence (XRF) analysis. The FA used in the study is classified as Class F with the total content of SiO_2, Al_2O_3, and Fe_2O_3 (86.6%) higher than 50%, the CaO content (6.42%) less than 18%, and LOI (3.48%) less than 6% according to ASTM C618-19 [42]. It is noted that the oxidation of sulfur-rich species in GGBS is the major reason for the negative LOI value obtained in the study [43]. The morphologies of these raw materials are shown in Fig. 1. Most of FA particles are spherical but some impurities exist with irregular shapes, while GGBS and cement particles almost have angular appearances. For silica fume, the particle size is much smaller than those of the other three powders. Fig. 2 shows the particle size distributions of these four types of raw materials.

Table 1
Chemical components of raw materials obtained from XRF (%).

Chemical composition	FA	GGBS	Cement	SF
Aluminum oxide, Al_2O_3	25.80	14.60	6.07	0.15
Silicon oxide, SiO_2	52.40	33.90	19.60	96.90
Calcium oxide, CaO	6.42	40.50	64.80	0.53
Ferric oxide, Fe_2O_3	8.40	0.30	3.01	0.06
Magnesium oxide, MgO	2.27	7.03	0.87	1.10
Sulfur trioxide, SO_3	0.86	2.23	4.24	0.12
Titanium dioxide, TiO_2	1.31	0.51	0.26	/
Phosphorus oxide, P_2O_5	0.66	0.13	0.13	0.33
Potassium oxide, K_2O	1.47	0.46	0.68	0.78
Others	0.41	0.34	0.34	0.03
LOI (950 °C)	3.48	−0.14	3.83	1.78

Anhydrous sodium metasilicate (Na_2SiO_3-Anhydrous) particles in industrial grade were purchased from Qingdao Haiwan Chemical Co., Ltd. and used as the solid activator. According to the supplier, the chemical compositions of the Na_2SiO_3-Anhydrous particles were 50.75% Na_2O, 46.52% SiO_2, and 2.73% impurities with a modulus ratio [$M = Mol (SiO_2)/Mol (Na_2O)$] of 0.94, and the particle size was 0.25–1.00 mm with the loose bulk density of 1.31 g/cm³.

Fine silica sand (FSS) with the water absorption and specific gravity of 0.8% and 2.67 (according to GB/T 14684–2011 [44]) was used to prepare the comparison samples for calorimetry test, BSE-EDS mapping, and microhardness test. The average particle size of fine silica sand was below 300 μm, which is widely used in high-strength ECC.

Ultra-high-molecular-weight polyethylene (PE) fibers with the strength, modulus, and density of 3000 MPa, 100 GPa, and 0.97 g/cm³, respectively, were used as the reinforcement in ECC. The PE fibers had a diameter of 24 μm and a length of 18 mm.

Polycarboxylate ether type super-plasticizer purchased from BASF was used in the high-strength ECC mix, and tap water was used in the production of both geopolymer aggregates and ECC.

2.2. Artificial geopolymer aggregates

The one-part mixing technology was used to produce GPA [23]. The precursor was prepared with FA and GGBS in the ratio of 80% and 20% by weight. The activator to precursor ratio was 0.12 and the water to precursor ratio was 0.35 by weight. First, FA, GGBS, and solid activator were added into a mixer and mixed for 5 min. Then, water was added into the mixer and the slurry was stirred for another 4 min. Afterwards, the fresh paste was poured into cubic molds (100 mm × 100 mm × 100 mm) and vibrated for 30 s. The specimens were demolded after 24 h, crushed into fragments smaller than 4.75 mm using a crushing machine, and then kept in sealed plastic bags for six-month storage. The particle size distribution of GPA used in the ECC is presented in Table 2 and the photograph of the prepared GPA is shown in Fig. 3. It is noted that the present work focuses on the feasibility of using GPA to modify the properties of ECC and the underlying mechanisms. Only one typical mix proportion of GPA was adopted for research. The blended use of GGBS and FA enables easy development of early strength of GPA. In addition, incorporating GGBS into geopolymer aggregates can enhance the aggregate/cementitious matrix interfacial bond [23]. The influence of the GPA compositions as well as the gradation effect on the performance of GPA-ECC is an issue for further study in the future.

The specific gravity of GPA was tested as 2.05 according to GB/T 14684–2011 [44], which is lower than that of fine silica sand (2.67). As the common water absorption testing method for natural sand may not be suitable for lightweight fine aggregates with high water absorption [45], a paper towel method proposed by the Department of Transportation for the State of New York was specially adopted for testing the water absorption of GPA [46]. The water content and water absorption values of GPA were tested as 19.2% and 24.6%, respectively, and the latter value is much higher than that of fine silica sand (0.8%). It should
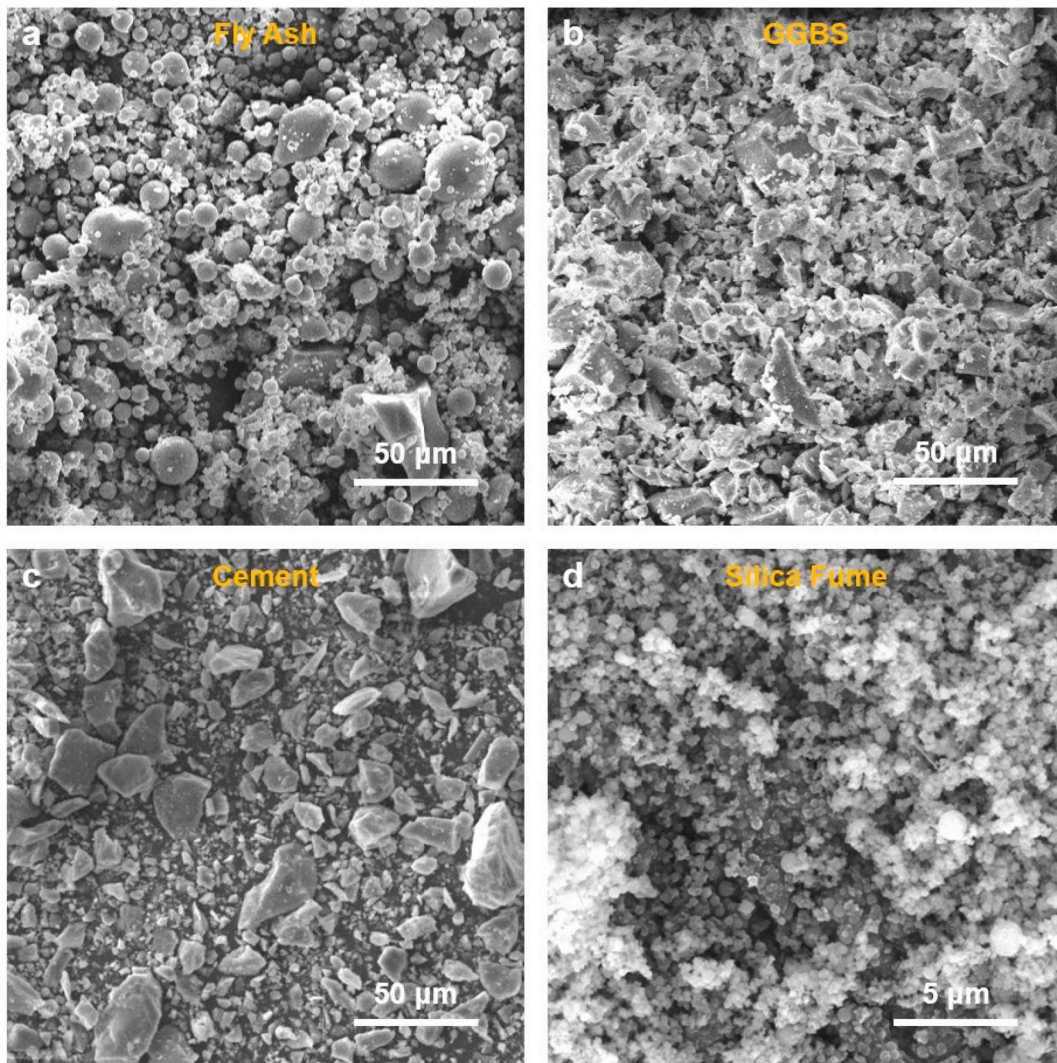
Fig. 1. SEM images of (a) fly ash, (b) GGBS, (c) cement, and (d) silica fume.

be pointed out that different mix proportions, production processes and curing schemes of GPA may result in different pore structures of GPA, which determine the corresponding water absorption ability. The high water absorption of GPA may make them possible to function as internal curing agents that influence the hydration process of the cementitious matrix of ECC. To measure the strength of GPA, six 20 mm × 20 mm × 20 mm cubes made in the same mix proportion with GPA were casted following the same production procedure until 28-day for compressive tests and the average strength of these cubes at 28 d was found to be 52.4 MPa.

2.3. Geopolymer aggregate ECC

In this study, the aggregate content was set as the variable in mixing ECC. Three GPA-ECC groups with different GPA contents were prepared (Table 3). In the mix design, the aggregate-to-binder ratios of GPA-ECC were set as 0.24, 0.48 and 0.72, respectively. It is noted that "SSD" in Table 3 means saturated surface dry (SSD) condition of GPA.

Before mixing the ECC, GPA were pre-wetted to the saturated surface dry (SSD) condition. Then, cement, silica fume and GPA were dry-mixed in a mixer for 5 min. Next, water and super-plasticizer were poured into the mixer and the mixture was stirred for another 10 min until a uniform paste appeared. After that, PE fibers were added into the mixer and the mixing was continued for another 5 min. After a uniform flowable ECC

was formed, three 50 mm × 50 mm × 50 mm cubes and three dumbbell samples (Fig. 4) were casted, respectively, and the specimens were covered by a plastic sheet to prevent water evaporation. After 24 h, the specimens were demolded and the demolding densities of GPA-ECC were measured (see Table 3). Then, the specimens were stored in water (23 °C) for 28 d until further tests.

2.4. Testing methods

Three 50 mm × 50 mm × 50 mm cubes were tested under compression for each mix proportion, according to ASTM C109/C109 M [47], and the loading rate was set as 1.0 MPa/s. Three dumbbell specimens were tested under direct tension for each mix, and the loading rate was set as 0.5 mm/min. During the tensile test, a linear variable differential transformer (LVDT) was fixed on one side of the specimen to measure the deformation of its central part (80-mm gauge length). On the other side, the digital image correlation (DIC) method [48–50] was adopted to obtain the whole strain field in the central area (see Fig. 4), where speckle pattern was sprayed in advance. During the test, a digital camera was used to capture photographs of the detected area at an interval of three seconds.

After the tensile test, small samples were carefully cut from the fracture surface of GPA-ECC and used for scanning electron microscope (SEM) analysis (Tescan VEGA3) to investigate the fiber failure modes in
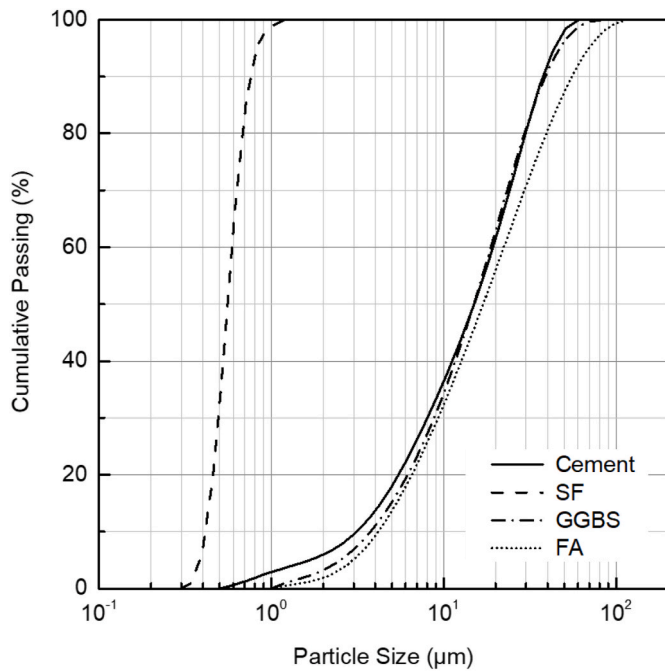
Fig. 2. Particle size distributions of raw materials.

cases of different ECC mix proportions.

Isothermal calorimetry tests (Calmetrix I-Cal 4000) were conducted to observe the effect of GPA on the early age hydration of ECC matrix, for which the A0.24 mix (excluding fibers) was used. Here, the other mix using fine silica sand as the aggregates was adopted as a reference following the same mix proportion. It should be noted that the aggregate volume contents of these two mixes were kept the same, and the result of the fine silica sand (in SSD)-to-binder ratio by weight was calculated as 0.253 based on the specific gravity of the aggregates. During the preparation, the matrices were mixed following the same procedure as shown in Section 2.3. Then, the fresh samples were weighed, put into plastic containers, and placed in the machine for 72 h. In the following analysis, the measured reaction heat was normalized with the weight of the tested matrix.

In the BSE test, a small sample of GPA-ECC (A0.24) was prepared, put into fresh epoxy resin, and vacuumed to remove the bubbles before the resin hardening. For comparison, a sample of fine silica sand mixture was also casted with the same mix as described in the isothermal calorimetry test. The cube was cured following the same procedure described in Section 2.3, cut into small samples, and prepared with fresh epoxy resin similar with that of GPA-ECC. Then, both types of samples were polished and coated with gold sputter. BSE tests were conducted with EDS mapping to observe the aggregate/matrix interfacial transition zone (ITZ) for both GPA-ECC (A0.24) and the fine silica sand counterpart. In the BSE mode, aggregates and matrix are easily identified as their elemental components are different. Two magnification levels of 1000 and 4000 times were selected, by which the aggregate/matrix ITZs were first found and then further localized. At the magnification level of 4000 times, element mapping in the EDS mode was conducted to investigate the aggregate/matrix ITZ.

In the microhardness test, the samples used in the BSE tests were further polished to remove the gold sputter layer, and the microhardness test was thereafter conducted. The aggregate/matrix ITZ, aggregates

(both silica sand and GPA) and matrix were selected as the target areas for the indentation test (Here, "matrix" denotes the blended cement and silica fume paste). It is noted that the indentation location on the aggregate and matrix was 15 μm away from the aggregate/matrix ITZ in order to prevent the overlapping of the indentation marks and reduce

Fig. 3. The photograph of geopolymer fine aggregates.

Table 3
Mix proportions of GPA-ECC (kg/m³).

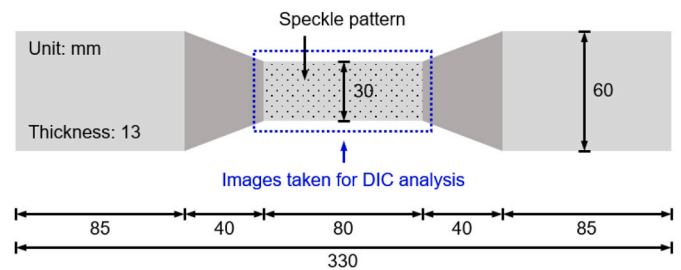| Raw Materials	GPA-ECC		
	A0.24	A0.48	A0.72
Cement	1191.0	1014.4	882.4
Silica Fume	297.8	253.6	220.6
SSD GPA (Dry GPA)	357.3 (287.3)	608.7 (488.2)	794.1 (637.5)
Water	254.6	216.8	188.6
Super-plasticizer (in solid)	19.4	16.5	14.3
PE Fiber (Vol %)	19.4	19.4	19.4
Demolding Density (g/cm³)	2.12	2.11	2.10

Fig. 4. Dumbbell specimen.

Table 2
Particle size distribution of GPA used for ECC casting.

Particle size (mm)	2.36–4.75	1.18–2.36	0.6–1.18	0.3–0.6	0.15–0.3	0–0.15
GPA	30%	28%	13%	10%	7%	12%

the influence of unexpected rigid/soft inclusion surface on the indentation depth of the indenter [51]. The loading force was kept as 0.098 N for the matrix, GPA, and their ITZ, while the force was changed to 0.490 N for silica sand because of the higher hardness in this area. For each sample, ten measurements were conducted to obtain the distribution of the hardness value.

Finally, small pieces of sample were cut away from the central part of the dumbbell specimens (A0.24, A0.48, and A0.72) after the tensile test, and the samples were scanned by a micro-focus X-ray CT system (YXLON FF35 CT). The 3D image of the scanned samples was reconstructed, and the voxel size of the CT image is 28.7 μm. Then, the internal cracking behavior and the size distributions of matrix flaws and GPA were analyzed using the ImageJ software.

3. Results and discussions

3.1. Mechanical properties

The mechanical properties of GPA-ECC (A0.24, A0.48 and A0.72) including compressive strength (f'_c), tensile strength (f_t), tensile strain capacity (ε_t), and average crack width at the ultimate tensile strain (w) are summarized in Fig. 5 and Table 4. The tensile stress–strain relations of GPA-ECC as well as the DIC strain fields are presented in Fig. 6.

In Fig. 5a, the compressive strengths of A0.24, A0.48, and A0.72 are 134.0 MPa, 120.7 MPa, and 116.9 MPa, respectively. The higher content of GPA resulted in a lower compressive strength, due to the relatively lower strength of GPA as compared with the high-strength matrix. In Fig. 5b, A0.48 showed the highest tensile strength, but the value dropped significantly when the aggregate-to-binder ratio increased to 0.72. The reduction of tensile strength may be related to the negative impact of the aggregate size (2.36–4.75 mm) on the uniformity of fiber distribution. In Fig. 5c, the tensile strain capacity of A0.48 reached 8.8%, while that of A0.72 was the lowest (6.5%). It is noted that high content of GPA (A0.72) led to a loss of tensile ductility (compared with A0.48 and A0.24) as the uniformity of fiber distribution in ECC matrix was significantly disturbed and the fiber bridging strength reduced. The small crack width of A0.72 (i.e., 40 μm at the ultimate strain) further reduced the tensile strain capacity. In addition, the GPA micro-spalling and the nonuniformity of fiber distribution caused by fiber/GPA interaction may influence the strain-hardening behavior of GPA-ECC. Fig. 5d shows the average crack width of each type of ECC at the ultimate tensile strain. The average crack width gradually decreased as the GPA content increased. Further discussion of the cracking behavior will be provided together with the DIC results. Table 4 presents the $f'_c f_t \varepsilon_t / w$ index [52],

Table 4
Mechanical properties of GPA-ECC.

Mechanical Properties	A0.24	A0.48	A0.72
Compressive strength, f'_c (MPa)	134.0 ± 3.2	120.7 ± 1.8	116.9 ± 2.0
Tensile ultimate strength, f_t (MPa)	8.6 ± 1.0	9.2 ± 0.8	6.1 ± 0.3
Tensile strain capacity, ε_t (%)	7.6 ± 0.8	8.8 ± 0.9	6.5 ± 0.8
Average crack width at the ultimate strain, w (μm)	65.0 ± 5.8	56.7 ± 3.1	39.5 ± 2.2
$f'_c f_t \varepsilon_t / w$ Index (MPa²/μm)	1.35	1.72	1.17

which is defined as f'_c (unit: MPa) × f_t (unit: MPa) × ε_t (unit: 1)/w (unit: μm), to assess the overall mechanical properties of GPA-ECC. A0.48 attained the highest index value (i.e., 1.72 MPa²/μm), indicating the best overall performance among the developed GPA-ECC in this study.

Fig. 6 shows the tensile stress-strain curves and the respective DIC patterns for the three GPA-ECC mix proportions. In the DIC patterns, the first strain level (0.2%) indicated the strain at the serviceability stage, the last strain level was the ultimate tensile strain, and the other two strain levels divided the whole strain range into three equal sections. Significant tensile strain-hardening and saturated multiple cracking could be observed for all the mixes, and A0.48 showed the highest tensile ductility. The saturated multiple cracking of GPA-ECC was related to the flaw effect [53–55] of geopolymer fine aggregates in high-strength ECC matrix. Similar phenomena were also reported when expanded shale [53,54] and coarse river sand [56] were used to reduce the overall toughness of the matrix. Although the strength of GPA was not low (i.e., 52.4 MPa), these aggregates could act as "additional flaws" in a high-strength matrix (e.g., over 130 MPa in this study). Such flaw effect will be further verified based on the microhardness and XCT results in the following sessions.

In Fig. 7, the compressive strength and tensile ductility of GPA-ECC in this study are plotted together with those of the high-strength ECC (HS-ECC) in the literature [57–65]. To be consistent, the data of heat-cured high-strength ECC were excluded, whose compressive strengths are usually higher. From Fig. 7, the GPA-ECC (A0.24, A0.48, and A0.72) showed a higher tensile ductility than most of the existing high-strength ECC. In addition, the tensile strain capacity of A0.48 (8.8%) recorded the highest value among the ambient-cured high-strength ECC in Fig. 7, indicating that the use of GPA is an effective method to improve the tensile ductility of high-strength ECC.

To observe the fiber failure modes, small pieces of samples were cut from the fracture surface of GPA-ECC specimens for the SEM test, and the results are shown in Fig. 8. Similar to the phenomenon observed in
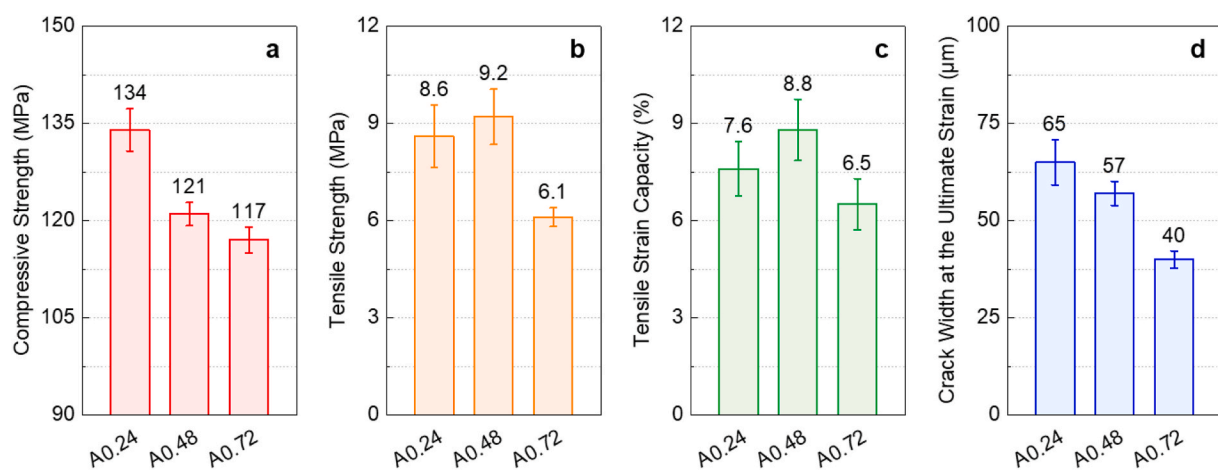

Fig. 5. Summary of mechanical properties of GPA-ECC (A0.24, A0.48 and A0.72): (a) Compressive strength, (b) tensile strength, (c) tensile strain capacity, and (d) average crack width at the ultimate strain. A0.48 exhibited the highest tensile strength and strain capacity. As the GPA content increased, the compressive strength and average crack width of GPA-ECC decreased.
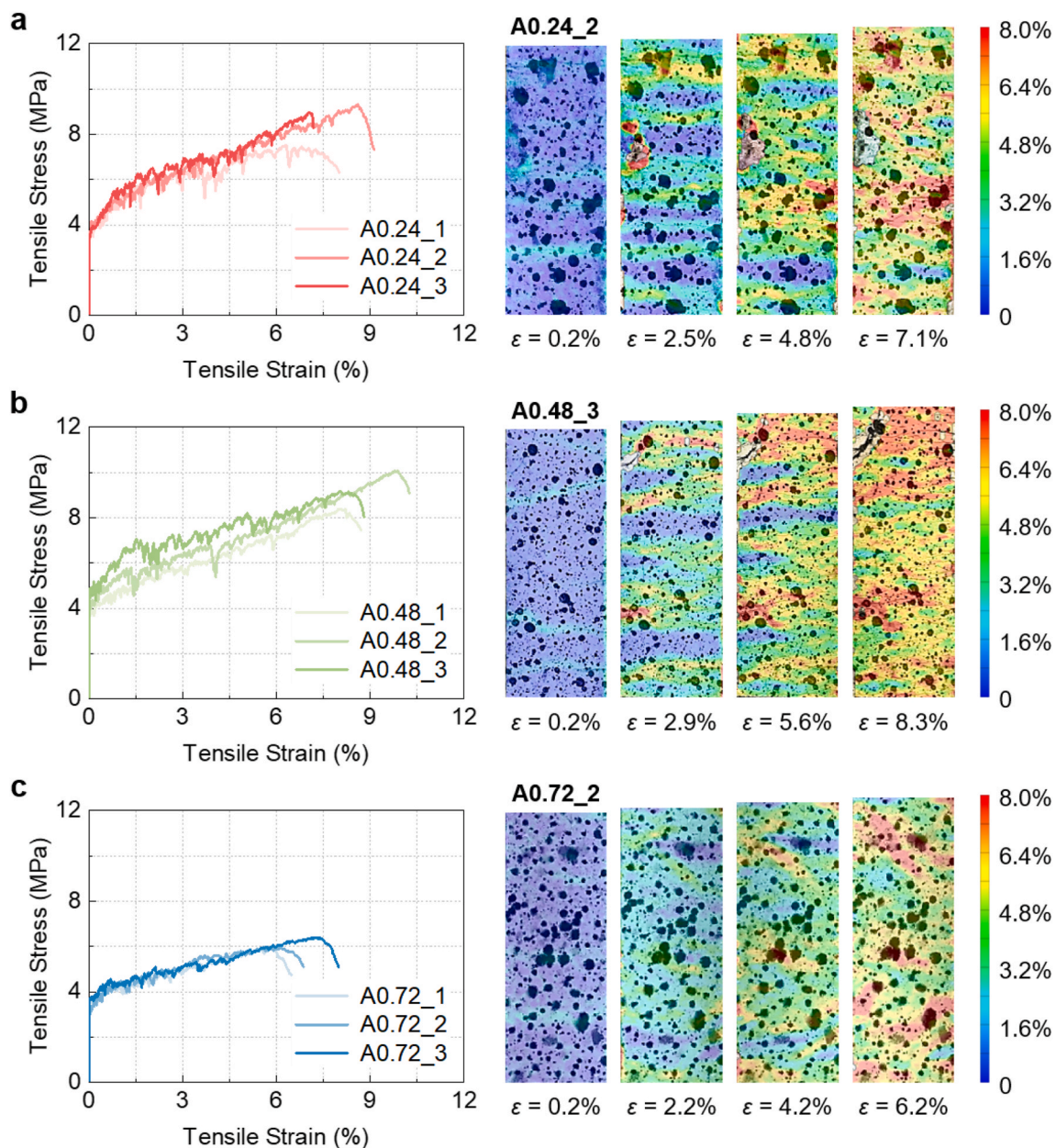
Fig. 6. Tensile stress–strain curves and DIC strain fields of GPA-ECC: (a) A0.24, (b) A0.48, and (c) A0.72. Significant tensile strain-hardening and multiple cracking can be observed for GPA-ECC, with A0.48 showing the highest tensile ductility. Color codes show local tensile strain values. (For interpretation of the references to colour in this figure legend, the reader is referred to the Web version of this article.)

ECC with fine silica sand and sea-sand [52,66], both fiber pullout and rupture failure could be observed. As the ultra-high-molecular-weight (PE) fibers had a high tensile strength, the rupture failure of the PE fibers means a strong fiber/matrix bond. Therefore, the rupture of some PE fibers indicates that the fiber strength was effectively utilized in GPA-ECC.

3.2. Hydration heat

Fig. 9 shows the comparison of heat release rate and cumulative heat produced during the early-stage hydration of GPA and fine silica sand (FSS) matrices for the first 72 h. As seen from the heat release rate curve, GPA matrix had an accelerated time to reach the peak of heat flow (19.5 h) as compared with the FSS matrix (22.0 h). Considering that the only difference between two matrices is the aggregate type and FSS is relatively inert, it is likely that the $Ca(OH)_2$ generated during the cement hydration might react with the existing GPA so that the pozzolanic reaction was promoted and thus generated the additional heat [40,67]. Moreover, since the one-part mixing method was used to produce GPA in this study, the solid activator content might not have dissolved completely. Therefore, a second time of mixing helped dissolve these remaining alkali activators which further activated the unreacted FA and GGBS particles in GPA, which resulted in more reaction heat. On the other hand, the descending branch of the heat release curve of GPA matrix dropped faster than that of FSS matrix, which was caused by the accelerated cement hydration in the GPA matrix. The heat release rates of these two ECC matrices became almost the same at 72 h, indicating that GPA had no further chemical reaction with the matrix when the matrix was fully hardened. In addition, the cumulative heat release of GPA matrix was found to be always higher than that of FSS matrix during the first 72 h (Fig. 9). At the end of the test, GPA matrix released more accumulated heat (4.3 J/g matrix) than FSS matrix, further
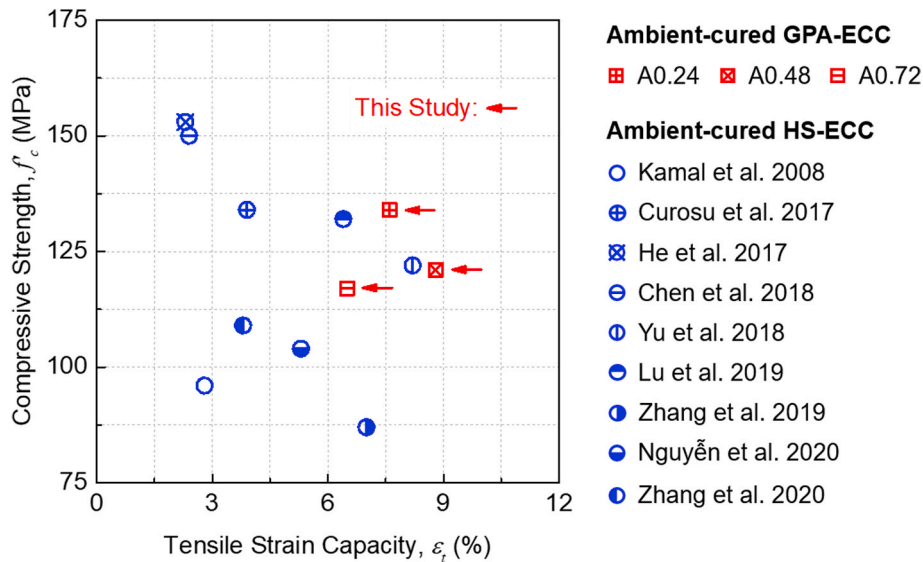
Fig. 7. Compressive strength and tensile strain capacity of high-strength ECC (HS-ECC) in the literature [57–65]. GPA-ECC exhibited superior tensile ductility.
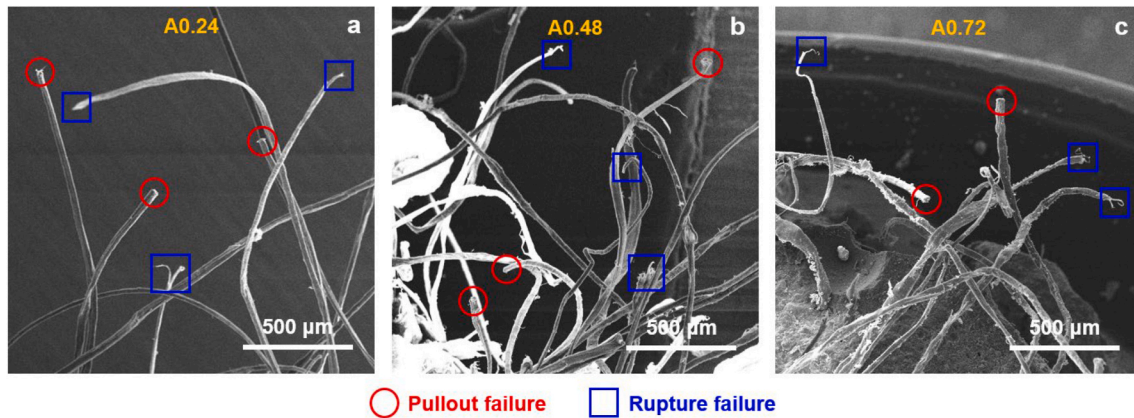

Fig. 8. SEM images of fiber failure modes: (a) A0.24, (b) A0.48, and (c) A0.72. Both rupture and pull-out ends can be observed.

verifying the occurrence of chemical reaction between the geopolymer aggregates and the matrix during the hydration process. Based on a previous study where alkali-activated binder was used as a repair material [67], the additional reaction product at the GPA/matrix ITZ was supposed to be C-A-S-H gel.

3.3. BSE-EDS analysis for aggregate/matrix ITZ

After the demonstration of the chemical reaction between GPA and the cementitious matrix in the previous section, BSE-EDS analysis was conducted to get a better understanding of the ITZ between the aggregates (GPA and silica sand) and the cementitious matrix. It should be noted here that because of the interactional chemical influence between GPA and the cementitious matrix, the ITZ defined here is a bit different from the conventional definition, where ITZ is only localized in the cementitious matrix. The microstructures of the GPA/matrix (A0.24) ITZ and its counterpart FSS/matrix ITZ are presented in Fig. 10 and 11, respectively.

In Fig. 10, many unreacted round particles (FA) are observed in the GPA region, which can help identify the boundary between the GPA and the cementitious matrix. The reasons for the existence of unreacted FA particles may be explained as follows: (1) The one-part mixing method of the aggregate paste cannot ensure sufficient alkali-activation of the precursors; and (2) GGBS has a higher alkaline reactivity than FA so that

GGBS will be consumed faster [40]. For the FSS/matrix ITZ in Fig. 11, the boundary between the FSS and the cementitious matrix is easier to distinguish, because the FSS is comparatively chemical-stable with a dense microstructure. It is noted that siliceous aggregates such as silica sand can also absorb certain amount of Ca^{2+} and OH^- ions if they stay in a simulated cement solution, and Si^{4+} will accordingly dissolve from the sand surface and then precipitate with new hydrated silicates formed [68]. Therefore, the FSS is not completely inert in the Ca-rich cementitious environment. In addition, several unreacted cement particles (light grey) can be found in the cementitious matrix (Fig. 10a and 11a). It can also be observed that the microcracks along the FSS/matrix ITZ are clearer than those along the GPA/matrix ITZ, indicating that the chemical bond in the latter case may be stronger than in the former case. The microcracks observed in both figures were supposed to arise from restrained shrinkage [69].

Figs. 10b and 11b present the magnified GPA/matrix and FSS/matrix ITZs, respectively. In order to make a clearer classification of the boundary, element mapping in the EDS mode was made for both ITZs. For the GPA mixture, although the Na element should be more abundant in GPA than in cement paste, the element distribution of Na was observed to be almost uniform in Fig. 10c, which was possibly due to the leaching of Na ions during mixing and curing. In addition, the Si element cannot be used to identify the ITZ, because both matrix (silica fume and cement) and GPA (FA, GGBS, and Na_2SiO_3) are composed of this
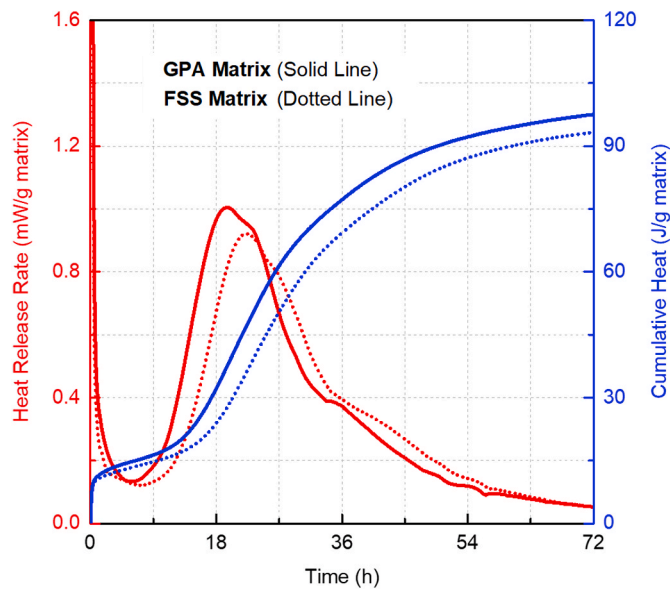
Fig. 9. Hydration heat of geopolymer aggregate (GPA) and fine silica sand (FSS) matrices. The use of GPA increased the hydration heat of cement and silica fume matrix during the first 72 h.

element. Therefore, Al (rich in GPA) and Ca (rich in cement) were used to identify the GPA/matrix ITZ (see Fig. 10d and f). For the FSS mixture, since FSS is mostly Si and cement is Ca-based, the FSS/matrix ITZ can be identified based on the mapping results of these two elements (see Fig. 11d and f).

For the ITZs in Fig. 10b and 11b, EDS linear scanning was conducted twice [Scanning (I) and Scanning (II)] to better understand the ion exchange in the GPA/matrix and FSS/matrix ITZs. For each scanning trace, the scanning was repeated five times to get a higher intensity and make the result more distinct. According to the scanning results, the variations of Al and Ca elements in the GPA/matrix ITZ are presented in Fig. 12a and b, while those of Ca and Si in the FSS/matrix ITZ are presented in Fig. 12c and d. From the linear mapping results, the ITZ ion exchange can be represented by element variations (i.e., the ascending and

descending parts of the curves in Fig. 12). As displayed in the figures, the widths of the GPA/matrix ITZ obtained along the two scanning traces were 6.9 μm and 7.0 μm, which are larger than those along the FSS/matrix ITZ (4.9 μm and 5.4 μm). As indicated in Ref. [70], the steeper ascending or descending of element intensity change means a less distinguished ion exchange at the aggregate/matrix ITZ. The width of GPA/matrix ITZ was larger than that of FSS/matrix ITZ, indicating that the newly formed ITZ products (C-A-S-H gels [67]) in the former case was more widely distributed than the hydrated silicates [68] formed in the latter case, because the Si dissolution from the silica sand is comparatively limited. This observation also coincided with the findings that less microcracks were observed along the GPA/matrix ITZ than the FSS/matrix ITZ in Fig. 10a and 11a, and the GPA had good bond with the cementitious matrix.

3.4. Microhardness of matrix, aggregate, and aggregate/matrix ITZ

To further verify the findings described in the above section, the hardness values (HV) of the aggregates (GPA and FSS), GPA/matrix ITZ, and cementitious matrix were measured by micro-indentation test. Here, it should be mentioned that the FSS/matrix ITZ was not tested, because the hardness difference between the FSS and the cementitious matrix is too large, leading to a large slippage of the indenter. Considering the stochastic nature of microhardness, ten measurements were conducted for each sample, and the Weibull distribution was used to fit the distribution of the measured hardness values. Table 5 summaries the fitted cumulative distributions. All the correlation coefficients were close to 1, indicating that the hardness values followed the Weibull distribution.

The distributions of the measured microhardness are shown in Fig. 13. The microhardness of GPA (average: 54.0 HV) was much smaller than that of the cementitious matrix (average: 85.6 HV). In other words, the GPA was significantly weaker than the matrix, and thus it would reduce the strength and fracture toughness of high-strength ECC matrix. Therefore, based on the micromechanical design principle, the crack tip toughness would also decrease with the addition of GPA, resulting in a more remarkable strain-hardening potential. In addition, the microhardness of GPA/matrix ITZ (average: 78.1 HV) was close to that of the matrix (average: 85.6 HV) and higher than that of GPA (average: 54.0 HV), indicating that the GPA/matrix ITZ was stronger than the GPA.
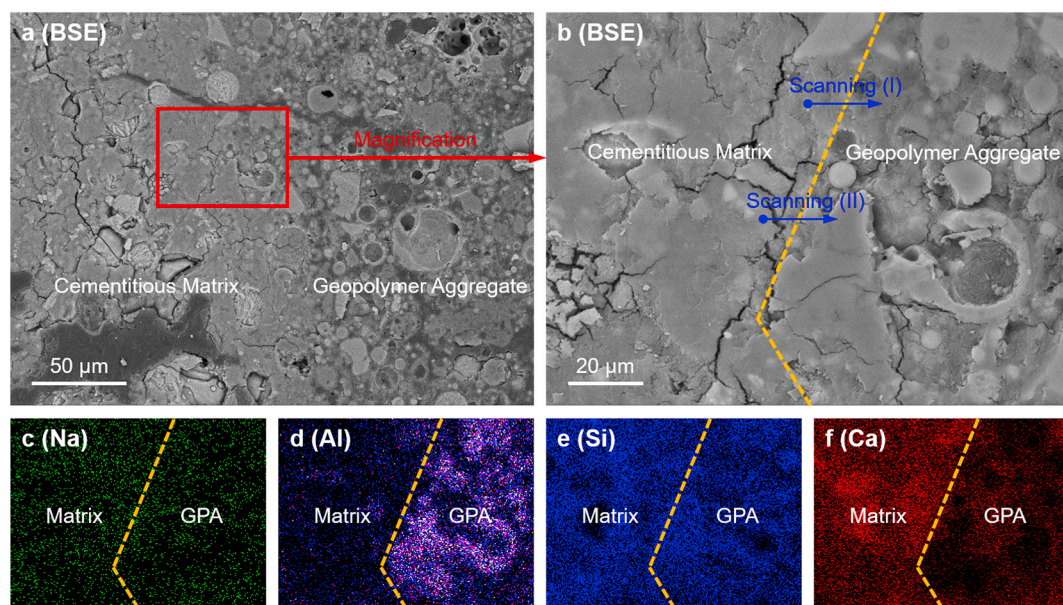

Fig. 10. BSE images (a and b) and elemental mapping results (c–f) of GPA/matrix ITZ. The GPA/matrix ITZ could be identified by the mapping results of Al and Ca elements.
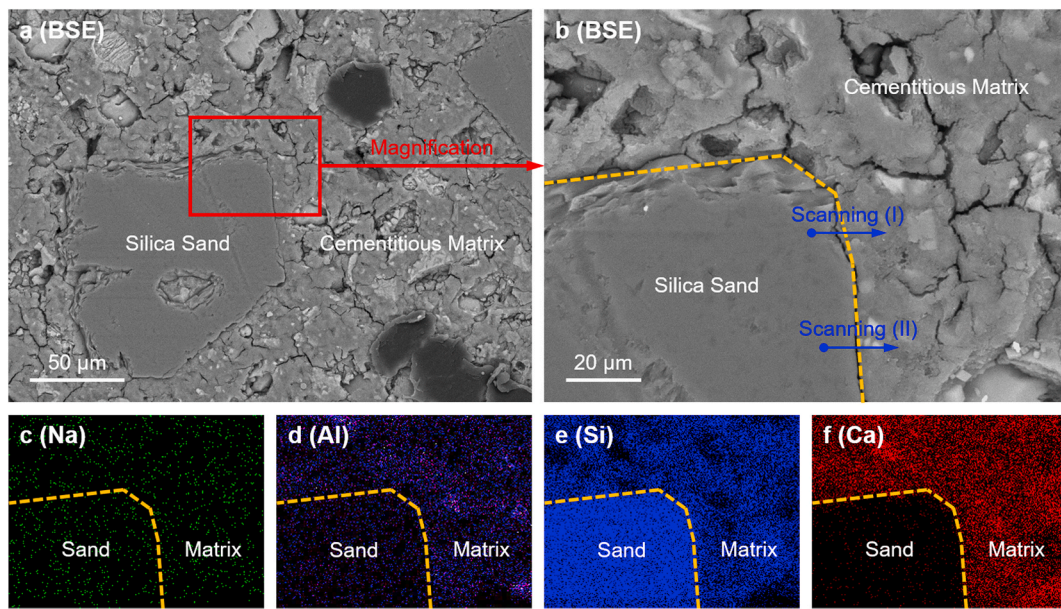
Fig. 11. BSE images (a and b) and elemental mapping results (c–f) of FSS/matrix ITZ. The FSS/matrix ITZ could be identified by the mapping results of Si and Ca elements.
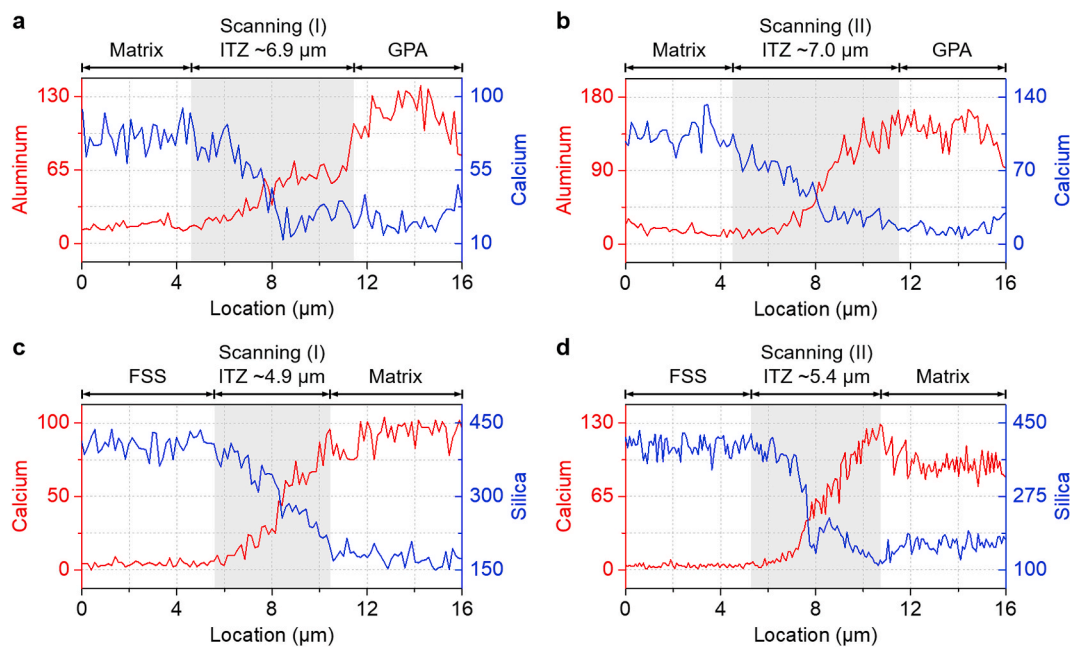

Fig. 12. Element variations of (a) Scanning (I) in Fig. 10, (b) Scanning (II) in Fig. 10, (c) Scanning (I) in Fig. 11, and (d) Scanning (II) in Fig. 11. The GPA/matrix ITZ seems to have a wider thickness (~7 μm) than that of the FSS/matrix ITZ (~5 μm).

Therefore, the strong ITZ is supposed to make cracks propagate through the weaker GPA instead of along the GPA/matrix interface under tension. For the FSS, the microhardness value was significantly larger than that of the matrix.

3.5. XCT result and flaw effect

Based on the findings in the previous sections, GPA are significantly weaker than the high-strength matrix. Thus, such artificial aggregates could be regarded as "additional flaws" in GPA-ECC. In this section, XCT analysis was conducted to gain an in-depth understanding of the flaw effect of GPA. Fig. 14 shows the reconstructed three-dimensional (3D) XCT images of cracked GPA-ECC (A0.24, A0.48, and A0.72) at the same

grayscale level. The internal cracks, initial flaws (i.e., pores), and GPA can be observed in the reconstructed XCT images, where the total volume of flaws (i.e., initial flaws and GPA) increased with GPA content. Here, only a small cube (5 mm × 5 mm × 5 mm) was shown in Fig. 14 in order to present the 3D XCT images clearly.

As it is difficult to clearly distinguish every initial flaw and GPA in the 3D XCT images of a comparatively large space, two-dimensional (2D) XCT images of GPA-ECC were used (Fig. 15) to quantify the distributions of initial flaws and GPA in ECC. It is noted that the area fraction of initial flaws and GPA in a 2D image is equal to the 3D volume fraction based on the stereology principles [71,72]. In the 2D XCT images (Fig. 15), the initial flaws (in black) and GPA (in dark grey) can be distinguished clearly. In Fig. 15, GPA-ECC showed more internal cracks

Table 5
Cumulative distributions of the measured microhardness values.

Test Area	Fitted Cumulative Distribution Function	Correlation Coefficient	Average Value (HV)
Geopolymer Aggregate	$F(x) = 1 - \exp(-(x/58.0)^{6.4})$	0.990	54.0
GPA/Matrix ITZ	$F(x) = 1 - \exp(-(x/82.2)^{9.7})$	0.995	78.1
Cementitious Matrix	$F(x) = 1 - \exp(-(x/91.3)^{7.4})$	0.983	85.6
Fine Silica Sand	$F(x) = 1 - \exp(-(x/1739.0)^{9.9})$	0.987	1654.0

Note: $F(x)$ is the cumulative distribution function of the measured microhardness value (x).

To analyze the size distribution of initial flaws and GPA in ECC, Fig. 16 presents the equivalent radius of the initial flaws and GPA obtained from the 2D XCT images (Fig. 15). Due to the limitation of resolution, the initial flaws smaller than 0.2 mm (radius ≤0.1 mm) and the GPA smaller than 0.4 mm (radius ≤0.2 mm) were not considered. It is noted that compared with the initial flaws (in black), the grayscale level of the GPA is much closer to that of the matrix, so the distinguishable minimum size of the GPA (i.e., 0.2 mm in radius) is larger than that of the initial flaws (i.e., 0.1 mm in radius). For ECC materials, the size distribution of initial flaws can be described by the following Weibull-type function [Eq. (1)] [73].

$$F(r) = 1 - \exp\left[-\left(\frac{\lambda}{r - r_0} \right)^k \right] \tag{1}$$

where $F(r)$ is the cumulative probability of initial flaws having an
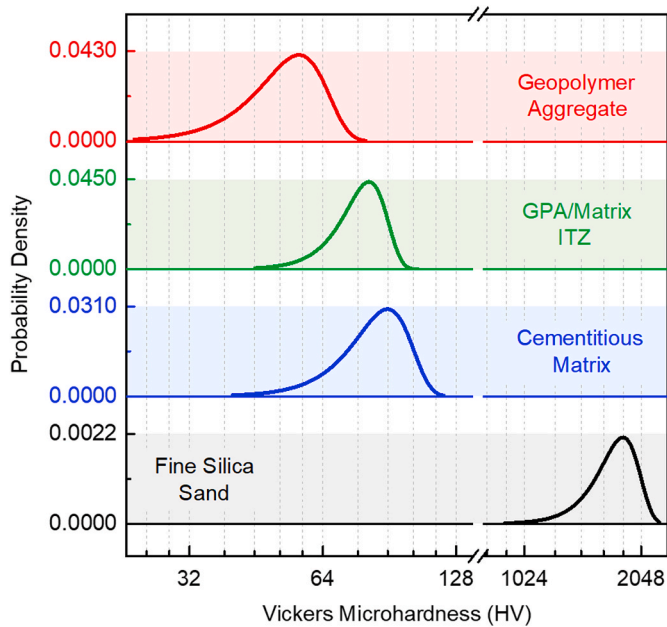

Fig. 13. Microhardness of aggregates (GPA and FSS), matrix, and GPA/matrix ITZ. The microhardness value of GPA/matrix ITZ was close to that of the cementitious matrix and higher than that of the GPA.

with increasing the GPA content and many cracks passed through the initial flaws and GPA, demonstrating the role of GPA as "additional flaws" in GPA-ECC. Moreover, almost no ITZ cracks could be observed around the GPA, indicating a good bond of the GPA/matrix ITZ.

Fig. 15. Two-dimensional XCT images of cracked GPA-ECC: (a) A0.24, (b) A0.48, and (c) A0.72. Many cracks passed through the GPA, and GPA-ECC showed more internal cracks with increasing GPA content.
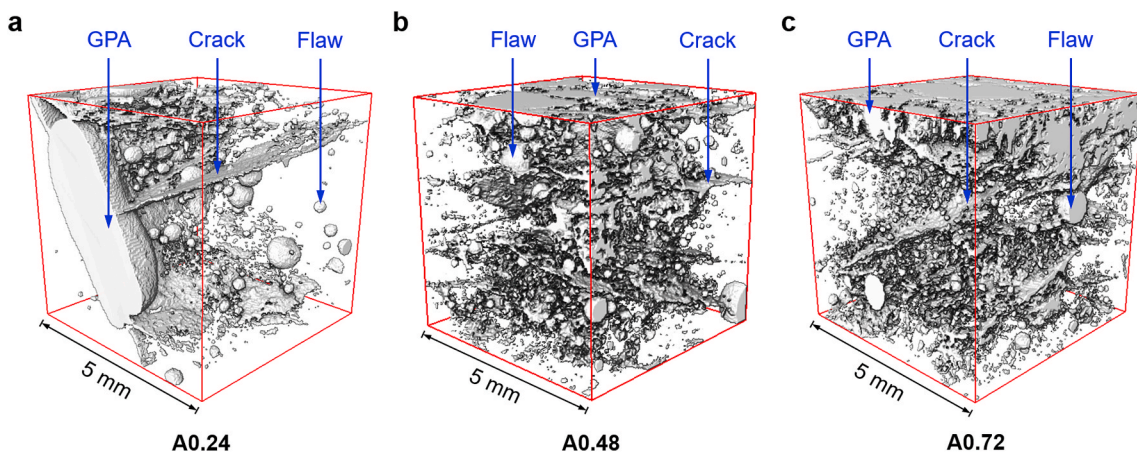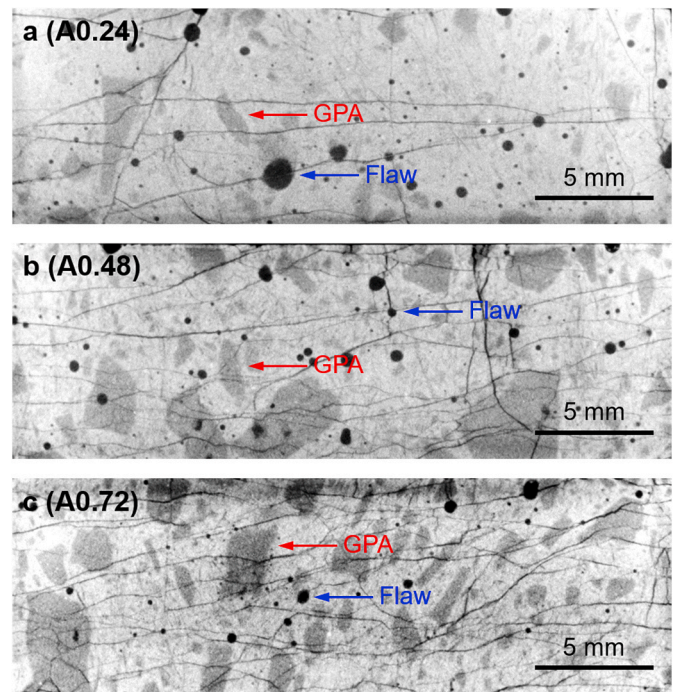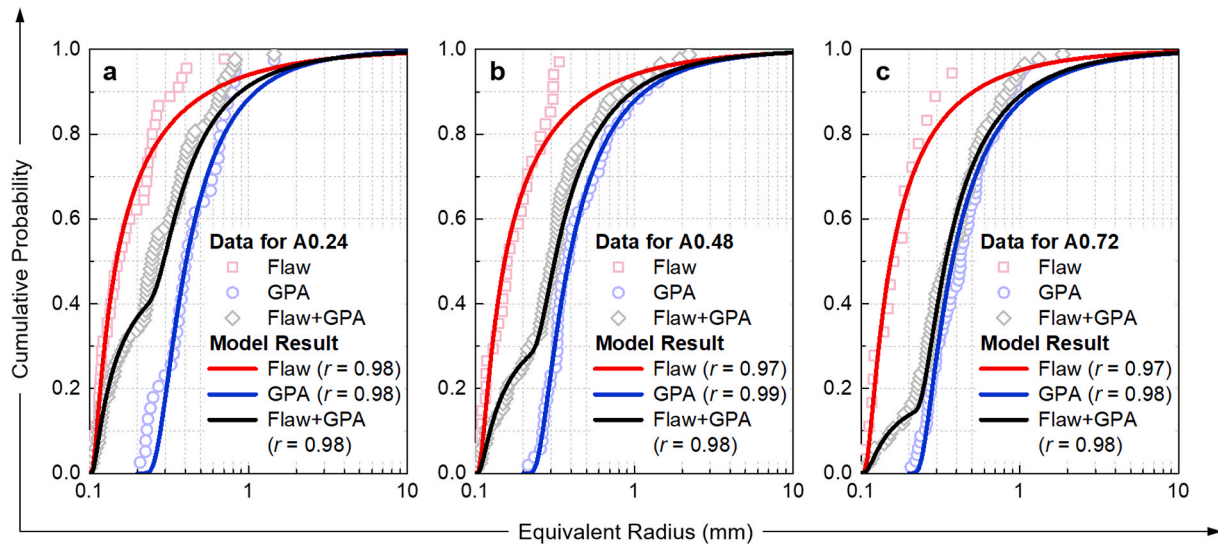

Fig. 14. Three-dimensional XCT images of cracked GPA-ECC: (a) A0.24, (b) A0.48, and (c) A0.72 at the same grayscale level. The internal cracks, flaws, and geopolymer aggregates could be observed in the reconstructed XCT images.

Fig. 16. Size distributions of initial flaws and GPA in ECC: (a) A0.24, (b) A0.48, and (c) A0.72. The model results showed good agreement with the measured results.

equivalent radius smaller than r, k is the shape parameter, λ is the scale parameter, and r_0 is the smallest flaw radius. In addition, Eq. (1) was used to model the size distribution of GPA. Table 6 lists the model results of the measured distributions of the initial flaws and GPA shown in Fig. 16. It seems that Eq. (1) can be applied to model the distributions of the initial flaws and GPA in ECC.

Based on the model results of the flaws and GPA, the distribution of the total flaws (i.e., flaw + GPA) can be calculated as follows:

$$F_{T}(r) = \frac{N_F}{N_F + N_A} F_F(r) + \frac{N_A}{N_F + N_A} F_A(r) \qquad (2)$$

where $F_F(r)$, $F_A(r)$, and $F_T(r)$ are the cumulative probability functions of the initial flaws, GPA, and total flaws, respectively; and N_F and N_A are the numbers of initial flaws and GPA. By introducing the distribution functions and numbers of initial flaws and GPA, the distributions of the total flaws could be obtained, which are presented in Fig. 16 and Table 6. It can be observed that the model results of Eq. (2) showed good agreement with the measured results and the correlation coefficients are close to 1, indicating the applicability of Eq. (2) in modeling the total

flaws in GPA-ECC.

Based on the model results in Table 6, the probability density functions (PDF) of the initial flaws, GPA, and total flaws (flaw + GPA) could also be obtained, which are plotted in Fig. 17. The first and second peaks of the total flaws represent the initial flaws and GPA, respectively. By incorporating different contents of GPA, the distribution of the total flaws changes significantly. For A0.24 and A0.48, the peak of the initial flaws was significantly higher than that of GPA, while for A0.72, the peak of the initial flaws was lower than that of GPA.

The comparison of the total flaw distributions in A0.24, A0.48, and A0.72 is shown in Fig. 18. As the content of GPA increased, the cumulative distribution function (CDF) shifted right, indicating that the use of GPA increased the size of the total flaws in high-strength ECC matrix. For example, the fractions of the total flaws larger than 0.5 mm (i.e., radius larger than 0.25 mm) were 58%, 68%, and 79% for A0.24, A0.48, and A0.72, respectively. In Fig. 18, the probabilistic density functions (PDF) of the total flaws in GPA-ECC were bimodal distributions, which are significantly different from the unimodal distribution of the flaws in ordinary ECC matrix [55]. It is evident that the GPA can be used to tailor the flaw size distribution of high-strength ECC matrix.

3.6. Summary of the ductility enhancement mechanism in GPA-ECC

Fig. 19 summarizes the ductility enhancement mechanism of high-strength ECC with GPA. According to the design theory of ECC, the larger the probability of active flaws is, the more easily multiple cracking phenomena can occur [53]. Here, active flaw means the flaw contributing to multiple cracking, i.e., flaws large enough to initiate crack extension at tensile stresses below the capacity of the bridging fibers. For high-strength GPA-ECC, GPA not only can achieve good bond with the cementitious matrix but also can act as "additional flaws" in the high-strength matrix. By incorporating GPA, it is feasible to increase the fraction of active flaws. As a result, more saturated multiple cracking as well as high tensile ductility can be achieved without debonding at the aggregate/matrix ITZ for high-strength ECC. It is noted that in the present study, GPA were used to tailor the flaw distribution in high-strength ECC matrix. For normal-strength ECC (e.g., 20–80 MPa), the strength grade of GPA may need to be tuned to realize the artificial flaw mechanism.

4. Conclusions

In this study, artificial geopolymer aggregates were used to develop

Table 6
Cumulative distributions of the initial flaws and GPA in ECC.

ECC	Function, F (r)	Number of Flaw & GPA, N	Distribution Parameters			Correlation
			λ	Coefficient, r	r_0	
A0.24	Flaw: $F_{F1}(r)$	$N_{F1} = 44$	0.030	0.82	0.1	0.98
	GPA: $F_{A1}(r)$	$N_{A1} = 38$	0.153	1.26	0.2	0.98
	Total Flaw (Flaw + GPA): $F_{T1}(r)$	$N_{T1} = N_{F1}$ $+ N_{A1}$	$F_{T1}(r) = (N_{F1}/N_{T1})F_{F1}(r) +$ $(N_{A1}/N_{T1})F_{A1}(r)$			0.98
A0.48	Flaw: $F_{F2}(r)$	$N_{F2} = 33$	0.035	0.86	0.1	0.97
	GPA: $F_{A2}(r)$	$N_{A2} = 51$	0.136	1.15	0.2	0.99
	Total Flaw (Flaw + GPA): $F_{T2}(r)$	$N_{T2} = N_{F2}$ $+ N_{A2}$	$F_{T2}(r) = (N_{F2}/N_{T2})F_{F2}(r) +$ $(N_{A2}/N_{T2})F_{A2}(r)$			0.98
A0.72	Flaw: $F_{F3}(r)$	$N_{F3} = 20$	0.036	0.92	0.1	0.97
	GPA: $F_{A3}(r)$	$N_{A3} = 47$	0.126	1.09	0.2	0.98
	Total Flaw (Flaw + GPA): $F_{T3}(r)$	$N_{T3} = N_{F3}$ $+ N_{A3}$	$F_{T3}(r) = (N_{F3}/N_{T3})F_{F3}(r) +$ $(N_{A3}/N_{T3})F_{A3}(r)$			0.98

Note: r_0 is determined by the distinguishable minimum sizes of the flaws ($r_0 = 0.1$ mm) and GPA ($r_0 = 0.2$ mm).
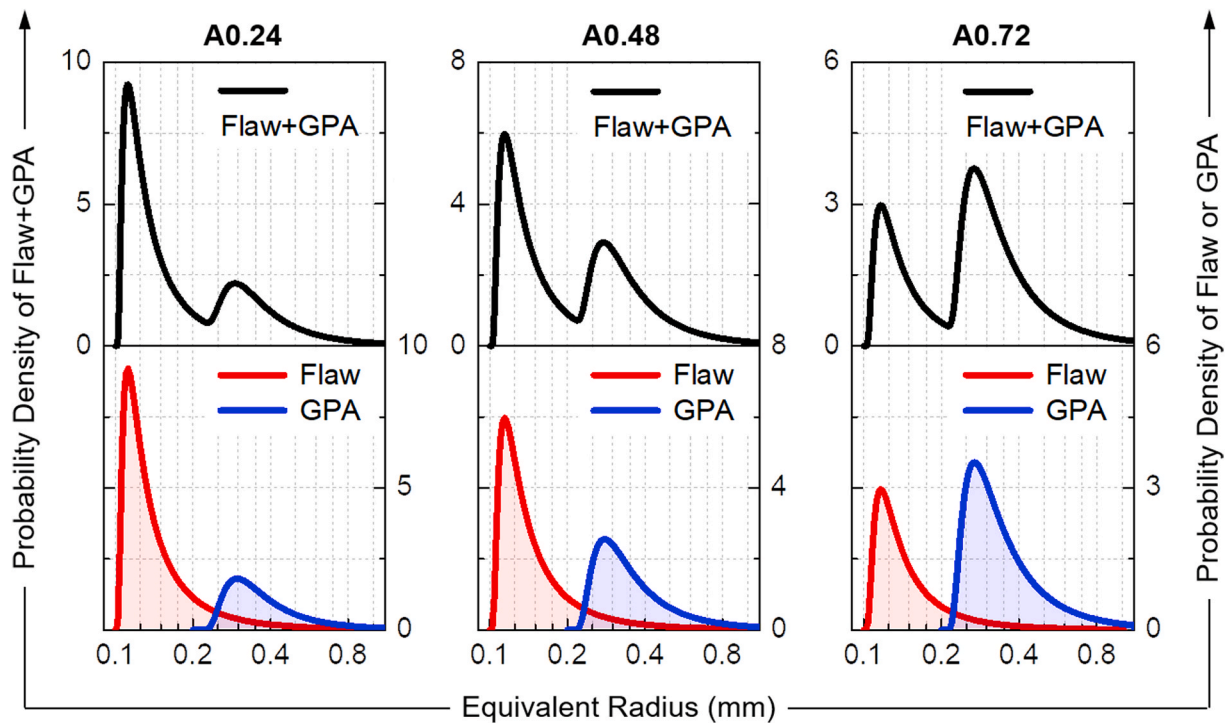
Fig. 17. Probability density functions of the initial flaws, GPA, and total flaws (flaw + GPA) in A0.24, A0.48, and A0.72. By incorporating different contents of GPA, the distribution of the total flaws changed significantly.
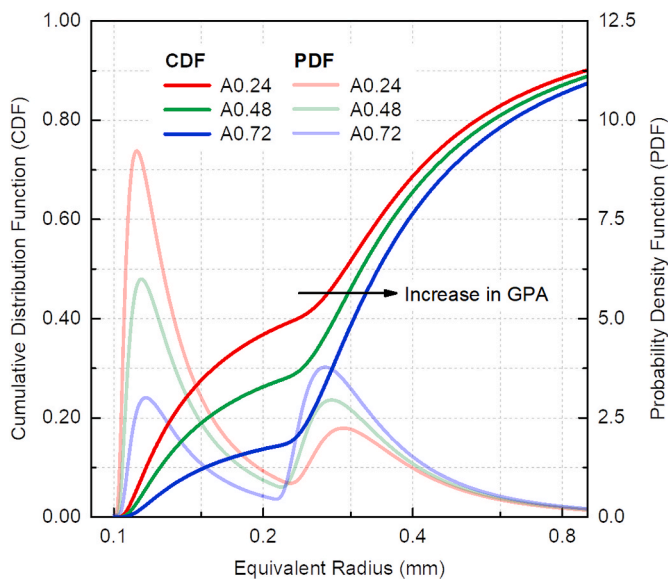

Fig. 18. Comparison of the cumulative distribution functions (CDF) and probability density functions (PDF) of the total flaws (flaw + GPA) in A0.24, A0.48, and A0.72. The distribution of the total flaws in high-strength matrix could be tailored by GPA.

high-strength high-ductility Engineered Cementitious Composites (ECC). A multi-scale investigation was conducted to better understand the microstructures and ductility enhancement mechanism of the geopolymer aggregate ECC (GPA-ECC). From the obtained results, the conclusions can be drawn as follows:

- For high-strength ECC, the use of geopolymer fine aggregates resulted in high tensile ductility and excellent crack control ability. For all the developed GPA-ECC, saturated multiple cracking behavior

could be observed with an average crack width below 70 μm (at the ultimate tensile strain). Compared with the ambient-cured high-strength ECC in literature, GPA-ECC showed superior tensile ductility, indicating that GPA can act as a material modifier for enhanced tensile ductility and crack control of high-strength ECC.

- The GPA reacted with the cementitious matrix (blended cement and silica fume). The GPA/matrix and FSS/matrix ITZs could be identified by Al and Ca elements, and Ca and Si elements, respectively. The width of the GPA/matrix ITZ (~7 μm) seemed to be larger than that of the FSS/matrix ITZ (~5 μm). In addition, the microhardness value of GPA/matrix ITZ was close to that of the cementitious matrix and higher than that of the geopolymer aggregate. The findings demonstrated that the GPA achieved a strong chemical bond with cementitious matrix and could be considered as "additional flaws" in high-strength matrix.

- The XCT results revealed that, many cracks passed through the GPA, demonstrating the role of GPA as "additional flaws" in ECC. The total distribution of initial flaws and GPA in ECC could be modeled based on a combination of two Weibull-type functions. By incorporating different contents of GPA, the flaw distribution of high-strength ECC changed significantly. The use of GPA can tailor the distribution of the total flaws (flaw + GPA) in high-strength ECC matrix, resulting in more saturated multiple cracking.

Further study is being conducted to understand the long-term mechanical performance of GPA-ECC to achieve a comprehensive understanding of this newly-developed material. In addition, it is suggested to further investigate the use of GPA in normal-strength concrete or ECC to explore the feasibility of using artificial aggregates for high performance cement-based materials. The durability properties, as well as the influence of different fibers [e.g., polyvinyl alcohol (PVA) fibers, polypropylene (PP) fibers, poly(p-phenylene-terephthalamide) (aramid) fibers, and as-spun poly(p-phenylene-2,6-benzobisoxazole) (PBO) fibers] on the mechanical properties of this new type of ECC should also be comprehensively investigated in the future. As sodium metasilicate production imposes certain burdens on the environment, for improved
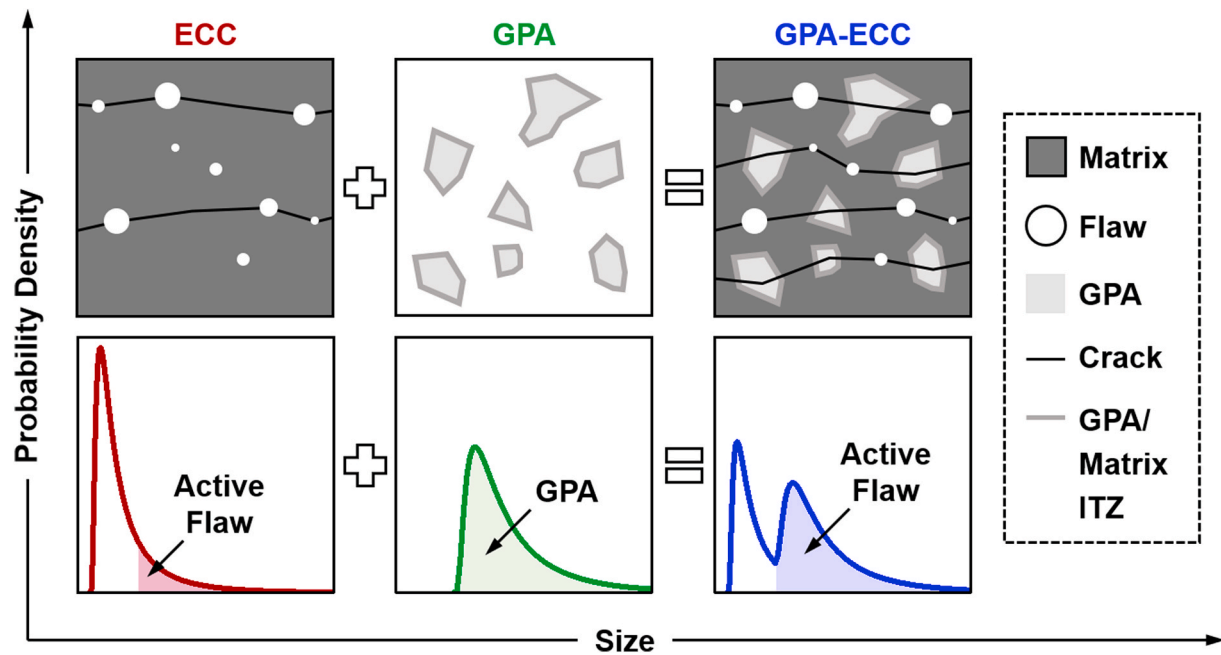
Fig. 19. Ductility enhancement mechanism for high-strength ECC with GPA. The use of GPA can tailor the flaw size distribution in high-strength matrix, resulting in a more saturated multiple cracking of ECC.

sustainability, more efforts are needed to explore alternative activators (especially from waste sources) to reduce carbon dioxide emission and global warming issues.

Credit author statement

LY Xu: Conceptualization, Methodology, Investigation, Formal analysis, Writing - Original Draft. **BT Huang**: Conceptualization, Methodology, Investigation, Visualization, Writing - Review & Editing. **VC Li**: Supervision, Writing - Review & Editing. **JG Dai**: Conceptualization, Funding Acquisition, Supervision, Writing - Review & Editing.

Declaration of competing interest

The authors declare that they have no known competing financial interests or personal relationships that could have appeared to influence the work reported in this paper.

Acknowledgments

References

[1] V.C. Li, Engineered Cementitious Composites (ECC) - Bendable Concrete for Sustainable and Resilient Infrastructure, Verlag GmbH Germany: Springer, Berlin, Heidelberg, 2019.

[2] J. Yu, J. Yao, X. Lin, H. Li, J.Y. Lam, C.K. Leung, K. Shih, Tensile performance of sustainable Strain-Hardening Cementitious Composites with hybrid PVA and recycled PET fibers, Cement Concr. Res. 107 (2018) 110–123.

[3] V.C. Li, C.K.Y. Leung, Steady-state and multiple cracking of short random fiber composites, J. Eng. Mech. 118 (11) (1992) 2246–2264.

[4] C.K.Y. Leung, Design criteria for pseudoductile fiber-reinforced composites, J. Eng. Mech. 122 (1) (1996) 10–18.

[5] B.T. Huang, Q.H. Li, S.L. Xu, B.M. Zhou, Frequency effect on the compressive fatigue behavior of ultrahigh toughness cementitious composites: experimental study and probabilistic analysis, J. Struct. Eng. 143 (8) (2017), 04017073.

[6] B.T. Huang, Q.H. Li, S.L. Xu, L. Zhang, Static and fatigue performance of reinforced concrete beam strengthened with strain-hardening fiber-reinforced cementitious composite, Eng. Struct. 199 (2019) 109576.

[7] B.T. Huang, Q.H. Li, S.L. Xu, B. Zhou, Strengthening of reinforced concrete structure using sprayable fiber-reinforced cementitious composites with high ductility, Compos. Struct. 220 (2019) 940–952.

[8] J. Zhou, J. Pan, C.K. Leung, Mechanical behavior of fiber-reinforced engineered cementitious composites in uniaxial compression, J. Mater. Civ. Eng. 27 (1) (2015), 04014111.

[9] B.T. Huang, Q.H. Li, S.L. Xu, W. Liu, H.T. Wang, Fatigue deformation behavior and fiber failure mechanism of ultra-high toughness cementitious composites in compression, Mater. Des. 157 (2018) 457–468.

[10] B.T. Huang, Q.H. Li, S.L. Xu, Fatigue deformation model of plain and fiber-reinforced concrete based on Weibull function, J. Struct. Eng. 145 (1) (2019), 04018234.

[11] J. Yu, H.L. Wu, C.K. Leung, Feasibility of using ultrahigh-volume limestone-calcined clay blend to develop sustainable medium-strength Engineered Cementitious Composites (ECC), J. Clean. Prod. 262 (2020) 121343.

[12] B.T. Huang, J. Yu, J.Q. Wu, J.G. Dai, C.K. Leung, Seawater sea-sand Engineered Cementitious Composites (SS-ECC) for marine and coastal applications, Composites Communications 20 (2020) 100353.

[13] B.T. Huang, Q.H. Li, S.L. Xu, B.M. Zhou, Tensile fatigue behavior of fiber-reinforced cementitious material with high ductility: experimental study and novel *P-S-N* model, Construct. Build. Mater. 178 (2018) 349–359.

[14] B.T. Huang, Y.T. Wang, J.Q. Wu, J. Yu, J.G. Dai, C.K. Leung, Effect of fiber content on mechanical performance and cracking characteristics of ultra-high-performance seawater sea-sand concrete (UHP-SSC), Adv. Struct. Eng. 24 (6) (2021) 1182–1195.

[15] K.Q. Yu, W.J. Zhu, Y. Ding, Z.D. Lu, J.T. Yu, J.Z. Xiao, Micro-structural and mechanical properties of ultra-high performance engineered cementitious composites (UHP-ECC) incorporation of recycled fine powder (RFP), Cement Concr. Res. 124 (2019) 105813.

[16] L. Wang, N.U. Rehman, I. Curosu, Z. Zhu, M.A.B. Beigh, M. Liebscher, V. Mechtcherine, On the use of limestone calcined clay cement (LC3) in high-strength strain-hardening cement-based composites (HS-SHCC), Cement Concr. Res. 144 (2021) 106421.

[17] B.T. Huang, J.Q. Wu, J. Yu, J.G. Dai, C.K. Leung, High-strength seawater sea-sand Engineered Cementitious Composites (SS-ECC): mechanical performance and probabilistic modeling, Cement Concr. Compos. 114 (2020) 103740.

[18] X. Huang, R. Ranade, W. Ni, V.C. Li, On the use of recycled tire rubber to develop low E-modulus ECC for durable concrete repairs, Construct. Build. Mater. 46 (2013) 134–141.

[19] X. Huang, R. Ranade, W. Ni, V.C. Li, Development of green engineered cementitious composites using iron ore tailings as aggregates, Construct. Build. Mater. 44 (2013) 757–764.

[20] A. Adesina, S. Das, Mechanical performance of engineered cementitious composite incorporating glass as aggregates, J. Clean. Prod. 260 (2020) 121113.

[21] Y. Zhou, G. Gong, Y. Huang, C. Chen, D. Huang, Z. Chen, M. Guo, Feasibility of incorporating recycled fine aggregate in high performance green lightweight engineered cementitious composites, J. Clean. Prod. 280 (2021) 124445.

[22] A. Torres, J. Brandt, K. Lear, J. Liu, A looming tragedy of the sand commons, Science 357 (6355) (2017) 970–971.

[23] L.Y. Xu, L.P. Qian, B.T. Huang, J.G. Dai, Development of artificial one-part geopolymer lightweight aggregates by crushing technique, J. Clean. Prod. 315 (2021) 128200.

[24] J. Thomas, B. Harilal, Sustainability evaluation of cold-bonded aggregates made from waste materials, J. Clean. Prod. 237 (2019) 117788.

[25] M.S. Nadesan, P. Dinakar, Structural concrete using sintered flyash lightweight aggregate: a review, Construct. Build. Mater. 154 (2017) 928–944.

[26] F. Tajra, M. Abd Elrahman, D. Stephan, The production and properties of cold-bonded aggregate and its applications in concrete: a review, Construct. Build. Mater. 225 (2019) 29–43.

[27] Paiva Yliniemi, Tiainen Ferreira, Illikainen, Development and incorporation of lightweight waste-based geopolymer aggregates in mortar and concrete, Construct. Build. Mater. 131 (2017) 784–792.

[28] J. Peyne, J. Gautron, J. Doudeau, S. Rossignol, Development of low temperature lightweight geopolymer aggregate, from industrial Waste, in comparison with high temperature processed aggregates, J. Clean. Prod. 189 (2018) 47–58.

[29] G. Habert, J.D.E. De Lacaillerie, N. Roussel, An environmental evaluation of geopolymer based concrete production: reviewing current research trends, J. Clean. Prod. 19 (11) (2011) 1229–1238.

[30] R. Pierrehumbert, There is no Plan B for dealing with the climate crisis, Bull. At. Sci. 75 (5) (2019) 215–221.

[31] L.A.T. Bui, C.L. Hwang, C.T. Chen, K.L. Lin, M.Y. Hsieh, Manufacture and performance of cold bonded lightweight aggregate using alkaline activators for high performance concrete, Construct. Build. Mater. 35 (2012) 1056–1062.

[32] U.S. Agrawal, S.P. Wanjari, D.N. Naresh, Characteristic study of geopolymer fly ash sand as a replacement to natural river sand, Construct. Build. Mater. 150 (2017) 681–688.

[33] P. Gomathi, A. Sivakumar, D. Singh, A. Rajaraman, V.M. Sounthararajan, Crushing strength properties of furnace slag-fly ash blended lightweight aggregates, ARPN Journal Engineering and Applied Sciences 8 (4) (2013) 246–251.

[34] P. Chindaprasirt, C. Jaturapitakkul, U. Rattanasak, Influence of fineness of rice husk ash and additives on the properties of lightweight aggregate, Fuel 88 (1) (2009) 158–162.

[35] K. Tian, Y. Wang, S. Hong, J. Zhang, D. Hou, B. Dong, F. Xing, Alkali-activated artificial aggregates fabricated by red mud and fly ash: performance and microstructure, Construct. Build. Mater. 281 (2021) 122552.

[36] M. Balapour, W. Zhao, E.J. Garboczi, N.Y. Oo, S. Spatari, Y.G. Hsuan, P. Billen, Y. Farnam, Potential use of lightweight aggregate (LWA) produced from bottom coal ash for internal curing of concrete systems, Cement Concr. Compos. 105 (2020) 103428.

[37] P.C. Lau, D.C.L. Teo, M.A. Mannan, Characteristics of lightweight aggregate produced from lime-treated sewage sludge and palm oil fuel ash, Construct. Build. Mater. 152 (2017) 558–567.

[38] J. Yliniemi, H. Nugteren, M. Illikainen, M. Tiainen, R. Weststrate, J. Niinimäki, Lightweight aggregates produced by granulation of peat-wood fly ash with alkali activator, Int. J. Miner. Process. 149 (2016) 42–49.

[39] E. Gomaa, A. Gheni, M.A. ElGawady, Repair of ordinary Portland cement concrete using ambient-cured alkali-activated concrete: interfacial behavior, Cement Concr. Res. 129 (2020) 105968.

[40] Y.S. Wang, K.D. Peng, Y. Alrefaei, J.G. Dai, The bond between geopolymer repair mortars and OPC concrete substrate: strength and microscopic interactions, Cement Concr. Compos. 119 (2021) 103991.

[41] L.Y. Xu, B.T. Huang, J.G. Dai, Development of engineered cementitious composites (ECC) using artificial fine aggregates, Construct. Build. Mater. 305 (2021) 124742.

[42] ASTM C618 – 19, Standard Specification for Coal Fly Ash and Raw or Calcined Natural Pozzolan for Use in Concrete, ASTM International, West Conshohocken, PA, 2019.

[43] M. Nedeljković, B. Ghiassi, S. van der Laan, Z. Li, G. Ye, Effect of curing conditions on the pore solution and carbonation resistance of alkali-activated fly ash and slag pastes, Cement Concr. Res. 116 (2019) 146–158.

[44] Chinese Standard GB/T 14684-2011, *Sand for Construction*, Standardization Administration of People's Republic of China, Beijing, China, 2011 (in Chinese).

[45] J. Castro, L. Keiser, M. Golias, J. Weiss, Absorption and desorption properties of fine lightweight aggregate for application to internally cured concrete mixtures, Cement Concr. Compos. 33 (10) (2011) 1001–1008.

[46] Test Method No.: NY 703-19 E, Moisture Content of Lightweight Fine Aggregate, New York State Department of Transportation, Materials Bureau, Albany, NY, 2008.

[47] ASTM C109/C109M, Standard Test Method for Compressive Strength of Hydraulic Cement Mortars, ASTM International, West Conshohocken, PA, 2013.

[48] B.T. Huang, Q.H. Li, S.L. Xu, C.F. Li, Development of reinforced ultra-high toughness cementitious composite permanent formwork: experimental study and digital image correlation analysis, Compos. Struct. 180 (2017) 892–903.

[49] B.T. Huang, J.G. Dai, K.F. Weng, J.X. Zhu, S.P. Shah, Flexural performance of UHPC-Concrete-ECC composite member reinforced by perforated steel plate, J. Struct. Eng. 147 (6) (2021) 04021065.

[50] Q.H. Li, X. Yin, B.T. Huang, A.M. Luo, Y. Lyu, C.J. Sun, S.L. Xu, Shear interfacial fracture of strain-hardening fiber-reinforced cementitious composites and concrete: a novel approach, Eng. Fract. Mech. 253 (2021) 107849.

[51] Y. Xu, Y.L. Wong, C.S. Poon, M. Anson, Impact of high temperature on PFA concrete, Cement Concr. Res. 31 (7) (2001) 1065–1073.

[52] B.T. Huang, K.F. Weng, J.X. Zhu, Y. Xiang, J.G. Dai, V.C. Li, Engineered/strain-hardening cementitious composites (ECC/SHCC) with an ultra-high compressive strength over 210 MPa, Composites Communications 26 (2021) 100775.

[53] S. Wang, V.C. Li, Tailoring of pre-existing flaws in ECC matrix for saturated strain hardening, in: Li (Ed.), Proceedings of FRAMCOS-5, 2004, pp. 1005–1012.

[54] V.C. Li, S. Wang, Microstructure variability and macroscopic composite properties of high performance fiber reinforced cementitious composites, Probabilist. Eng. Mech. 21 (3) (2006) 201–206.

[55] C. Lu, V.C. Li, C.K. Leung, Flaw characterization and correlation with cracking strength in Engineered Cementitious Composites (ECC), Cement Concr. Res. 107 (2018) 64–74.

[56] Y. Li, X. Guan, C. Zhang, T. Liu, Development of high-strength and high-ductility ECC with saturated multiple cracking based on the flaw effect of coarse river sand, J. Mater. Civ. Eng. 32 (11) (2020), 04020317.

[57] Z. Zhang, F. Yang, J.C. Liu, S. Wang, Eco-friendly high strength, high ductility engineered cementitious composites (ECC) with substitution of fly ash by rice husk ash, Cement Concr. Res. 137 (2020) 106200.

[58] Z. Zhang, A. Yuvaraj, J. Di, S. Qian, Matrix design of light weight, high strength, high ductility ECC, Construct. Build. Mater. 210 (2019) 188–197.

[59] K.Q. Yu, J.T. Yu, J.G. Dai, Z.D. Lu, S.P. Shah, Development of ultra-high performance engineered cementitious composites using polyethylene (PE) fibers, Construct. Build. Mater. 158 (2018) 217–227.

[60] Z. Lu, R. Yin, J. Yao, C.K. Leung, Surface modification of polyethylene fiber by ozonation and its influence on the mechanical properties of Strain-Hardening Cementitious Composites, Compos. B Eng. 177 (2019) 107446.

[61] H.H. Nguyễn, J.I. Choi, S.E. Park, S.L. Cha, J. Huh, B.Y. Lee, Autogenous healing of high strength engineered cementitious composites (ECC) using calcium-containing binders, Construct. Build. Mater. 265 (2020) 120857.

[62] I. Curosu, M. Liebscher, V. Mechtcherine, C. Bellmann, S. Michel, Tensile behavior of high-strength strain-hardening cement-based composites (HS-SHCC) made with high-performance polyethylene, aramid and PBO fibers, Cement Concr. Res. 98 (2017) 71–81.

[63] Y. Chen, J. Yu, C.K. Leung, Use of high strength strain-hardening cementitious composites for flexural repair of concrete structures with significant steel corrosion, Construct. Build. Mater. 167 (2018) 325–337.

[64] S. He, J. Qiu, J. Li, E.H. Yang, Strain hardening ultra-high performance concrete (SHUHPC) incorporating CNF-coated polyethylene fibers, Cement Concr. Res. 98 (2017) 50–60.

[65] A. Kamal, M. Kunieda, N. Ueda, H. Nakamura, Evaluation of crack opening performance of a repair material with strain hardening behavior, Cement Concr. Compos. 30 (10) (2008) 863–871.

[66] B.T. Huang, J.Q. Wu, J. Yu, J.G. Dai, C.K. Leung, V.C. Li, Seawater sea-sand engineered/strain-hardening cementitious composites (ECC/SHCC): assessment and modeling of crack characteristics, Cement Concr. Res. 140 (2021) 106292.

[67] A.M. Aguirre-Guerrero, R.A. Robayo-Salazar, R.M. de Gutiérrez, A novel geopolymer application: coatings to protect reinforced concrete against corrosion, Appl. Clay Sci. 135 (2017) 437–446.

[68] W.A. Tasong, J.C. Cripps, C.J. Lynsdale, Aggregate-cement chemical interactions, Cement Concr. Res. 28 (7) (1998) 1037–1048.

[69] J. Zhang, C. Gong, Z. Guo, M. Zhang, Engineered cementitious composite with characteristic of low drying shrinkage, Cement Concr. Res. 39 (4) (2009) 303–312.

[70] W.K.W. Lee, J.S.J. Van Deventer, Chemical interactions between siliceous aggregates and low-Ca alkali-activated cements, Cement Concr. Res. 37 (6) (2007) 844–855.

[71] E. Underwood, Quantitative Stereology, Reading Addison-Wesley Publishing Co., Boston, MA, USA, 1970.

[72] M. Nedeljković, B. Ghiassi, G. Ye, Role of curing conditions and precursor on the microstructure and phase chemistry of alkali-activated fly ash and slag pastes, Materials 14 (8) (2021) 1918.

[73] H.C. Wu, V.C. Li, Stochastic process of multiple cracking in discontinuous random fiber reinforced brittle matrix composites, Int. J. Damage Mech. 4 (1) (1995) 83–102.